Review of Scientific Instruments

Combining electron spin resonance spectroscopy with scanning tunneling microscopy at high magnetic fields

Cite as: Rev. Sci. Instrum. **93**, 043705 (2022); https://doi.org/10.1063/5.0078137
Submitted: 10 November 2021 • Accepted: 21 March 2022 • Published Online: 11 April 2022

Robert Drost, Maximilian Uhl, Piotr Kot, et al.

Review of Scientific Instruments ARTICLE scitation.org/journal/rsi

Combining electron spin resonance spectroscopy with scanning tunneling microscopy at high magnetic fields

Cite as: Rev. Sci. Instrum. 93, 043705 (2022); doi: 10.1063/5.0078137
Submitted: 10 November 2021 • Accepted: 21 March 2022 •
Published Online: 11 April 2022

Robert Drost,[1] Maximilian Uhl,[1] Piotr Kot,[1] Janis Siebrecht,[1] Alexander Schmid,[2] Jonas Merkt,[2] Stefan Wünsch,[2] Michael Siegel,[2] Oliver Kieler,[3] Reinhold Kleiner,[4] and Christian R. Ast[1,a)]

AFFILIATIONS

[1] Max-Planck-Institute for Solid State Research, Heisenbergstr. 1, 70569 Stuttgart, Germany
[2] Institut für Mikro- und Nanoelektronische Systeme, Karlsruhe Institute of Technology, Hertzstr. 16, 76187 Karlsruhe, Germany
[3] Physikalisch-Technische Bundesanstalt, Bundesallee 100, 38116 Braunschweig, Germany
[4] Physikalisches Institut, Center for Quantum Science (CQ) and LISA+, Universität Tübingen, 72076 Tübingen, Germany

[a)] **Author to whom correspondence should be addressed:** c.ast@fkf.mpg.de

ABSTRACT

The continuous increase in storage densities and the desire for quantum memories and computers push the limits of magnetic characterization techniques. Ultimately, a tool that is capable of coherently manipulating and detecting individual quantum spins is needed. Scanning tunneling microscopy (STM) is the only technique that unites the prerequisites of high spatial and energy resolution, low temperature, and high magnetic fields to achieve this goal. Limitations in the available frequency range for electron spin resonance STM (ESR-STM) mean that many instruments operate in the thermal noise regime. We resolve challenges in signal delivery to extend the operational frequency range of ESR-STM by more than a factor of two and up to 100 GHz, making the Zeeman energy the dominant energy scale at achievable cryogenic temperatures of a few hundred millikelvin. We present a general method for augmenting existing instruments into ESR-STM to investigate spin dynamics in the high-field limit. We demonstrate the performance of the instrument by analyzing inelastic tunneling in a junction driven by a microwave signal and provide proof of principle measurements for ESR-STM.

I. INTRODUCTION

The direct manipulation and detection of individual spins [see Fig. 1(a)] is one of the major goals in contemporary nanoscience.[1–9] Meeting these challenges requires a local measurement of electronic and magnetic properties with atomic precision. The scanning tunneling microscope (STM) routinely achieves this limit of resolution and is thus an excellent tool to study the dynamics of magnetic nano-objects[10] on their own length and time scales.[11–14]

Combining electron spin resonance with STM (ESR-STM) has introduced new possibilities to the local studies of individual spins and has expanded the available parameter space substantially, but it imposes a series of strict experimental requirements, most notably on the base temperature of the cryostat. The operational frequency range of the instrument determines the maximum magnetic field for ESR-STM experiments and sets the relevant energy scale in the experiment. ESR-STM relies on the thermal initialization of the target systems into their ground state. However, in many contemporary implementations of ESR-STM, the Zeeman energy is on the order of $k_B T$ and a non-negligible excited state population remains.[4,6] This is a significant impediment to resolving intrinsic spin dynamics at the nanoscale. The goal of coherent manipulation from a known ground state may be reached via two approaches: reducing the base temperature of the experiment to suppress thermal excitations from the ground state, or increasing the microwave frequency to operate at higher magnetic fields.

Current implementations of ESR-STM typically operate at frequencies up to 40 GHz.[15–17] To achieve thermal initialization of the target systems at these frequencies, mK temperatures are required, which are only achievable in dilution refrigerators.[18] This approach

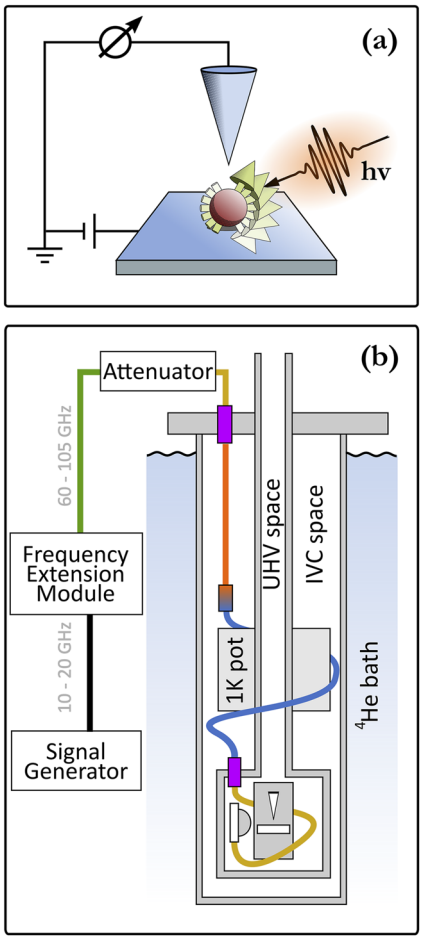

FIG. 1. (a) Principle of an ESR-STM measurement: an external microwave signal induces spin precession in a magnetic atom probed by the STM tip. (b) Sketch of the cryostat insert housing the STM with the RF wiring and antenna we installed in the system. Black lines indicate SMA cables, green lines are WR-12 wave guides, yellow lines are flexible 0.047 cables, orange lines are Cu/SPCW 0.047 semirigid cables, and blue lines are superconducting NbTi/NbTi 0.047 semirigid cables. Feedthroughs are indicated in purple. The ^{3}He stage is omitted for clarity.

requires dedicated machines that are costly to produce and present significant challenges in everyday operation. High frequency signals in the upper GHz range, on the other hand, can be generated in an independent setup outside the ultra-high vacuum (UHV) system and routed to the tunnel junction through a set of suitable cables. This approach is, therefore, more flexible, allowing the retrofitting or modification of existing machines by the addition of dedicated high GHz cabling.[19] Nevertheless, going to higher frequencies becomes increasingly challenging such that the use of coaxial cables is no longer feasible for frequencies above 110 GHz, where they have to be replaced by wave guides.

Extending the operational frequency range of ESR-STM has thus far been prevented by challenges in signal delivery. Approaching 110 GHz introduces increasing difficulties such as significantly higher intrinsic losses in the cabling, more stringent impedance matching, phase matching, and impedance conversion (antennae), as well as a greatly reduced commercial availability of ultrahigh vacuum compatible high frequency components. We will outline these challenges below and present corresponding solutions. We have augmented a commercially available STM (Unisoku model USM1300) featuring 310 mK base temperature and a 6 T single axis magnet with an antenna assembly that permits us to deliver microwave signals of up to 105 GHz directly to the tunnel junction. This work can be used as a guideline to design new instruments or retrofit existing ones for high GHz microwave capabilities.

II. INSTRUMENT DESIGN

The Unisoku model USM1300 STM is a commercially available experimental platform combining ultrahigh vacuum (UHV) sample preparation and ultra-low temperature STM with high field capabilities. The STM unit, developed and manufactured by the Unisoku corporation, is installed on the insert of a superinsulated ^{4}He bath cryostat produced by Cryogenic Ltd. The insert includes a 1 K pot, which is supplied with liquid helium from the bath through an adjustable needle valve, and a single-shot ^{3}He cooling cycle. With a total volume of 30 l ^{3}He gas, the STM is capable of operating at a base temperature of 310 mK for up to 72 h. In addition, all the non-RF wiring (bias voltage, tunneling current, piezo signals, etc.) are filtered by standard low pass filters supplied by Unisoku. Similar versions of such filters are described in Ref. 20.

Figure 1(b) shows a sketch of the cryostat insert including the modifications we implemented as part of the ESR-STM augmentation. The main addition to the base setup is the installation of a series of 0.047 in. semirigid coaxial cables, rated to 110 GHz, and a radio frequency antenna into the system. We solve the challenges of finding leak-tight vacuum feedthroughs and thermalization of the RF assembly to produce a high-performance machine capable of delivering high-frequency signals at large amplitudes onto the tunnel junction. Our approach extends the operational frequency range of ESR-STM by a factor of more than two while maintaining signal amplitudes comparable with previous efforts. Below is a step-by-step discussion of the design philosophy and implementation of our custom modifications to the base system.

A. High-frequency wiring

The geometry of STMs presents a severe challenge to the integration of high-frequency signals. The confined space of the scanner housing and the complex shape of the tip-sample system thwart any attempt to realize an impedance-matched connection to the tip. The resulting scattering of electromagnetic waves in the instrument will inevitably lead to high losses. This makes it all the more difficult to bring a high amplitude signal close to the tunnel contact. The requirement for high signal amplitudes leads to a conflict with a key design principle for cryostats to use high-resistance cabling in order to limit the thermal load on the experiment.

We overcome these issues by using a combination of high conductance coaxial cables from different materials to achieve maximum power transmission to the antenna. We use semirigid cables with a copper jacket and silver-plated copper weld (SPCW) conductor in the upper sections of the cryostat to the 1 K-pot [see the red

wire section in Fig. 1(b)]. Their high conductance ensures small signal losses even at room temperature. We installed a coaxial cable with an NbTi shield and a conductor running from the 1 K-pot to the ^{3}He stage [see the blue wire section in Fig. 1(b)]. NbTi is a superconductor with a transition temperature of 10 K and a high critical field of 15 T. As superconductors are excellent conductors of electricity but very poor conductors of heat,[21] the NbTi cable provides excellent signal transmission at low temperatures while essentially eliminating thermal loads on the low-temperature parts of the experiment. Finally, a flexible coaxial cable with a silver plated copper shield and conductor connects the RF antenna in order to preserve STM motion during sample transfer and spring damping during regular operation.

We use semirigid coaxial cables with 0.047 in. outer diameter for all applications. This cabling standard is rated to 110 GHz with an impedance of 50 Ω. We installed 1 mm connectors (Anritsu W1 series), also rated to 110 GHz, on all cable segments. Before installation in the machine, all cables were repeatedly immersed in liquid helium and rigorously tested for any temperature related damages.

Our combination of copper/SPCW and superconducting cables requires excellent heat management in order to work effectively. To ensure proper thermalization, all cables are anchored at several points inside the cryostat. The thermal anchors consist of a copper braid, glued to the outer conductor of the cable over a large surface area using thermally conductive silver epoxy and fastened to the anchor points with a screw and lug. The copper/SPCW cable is anchored at the baffles of the cryostat, the sorption pump, and the 1 K-pot. The NbTi cable is thermally anchored at the 1 K-pot and ^{3}He-pot as described above and wound in a wide loop around the UHV column to accommodate the thermal expansion and contraction of the wiring during cool-down or warm-up. The installation of our custom radio frequency cabling did not affect the base temperature of the instrument.

B. High-frequency UHV feedthrough

To our knowledge, there are no commercially available hermetically sealed double ended coaxial vacuum feedthroughs rated to 90 GHz or above. In practice, however, vacuum feedthroughs with 1.85 mm connectors, rated to 65 GHz, show very low losses up to at least 90 GHz and can act as a substitute. Figure 2 shows transmission measurements through the hermetically sealed feedthrough KPC185FFHA by Kawashima Manufacturing Corporation from 60 to 90 GHz. The performance of KPC185FFHA is comparable to 1 mm female–female adapters rated to 110 GHz. A pair of 1.85–1 mm adapters (e.g., CentricRF C8186) is needed to mate the feedthrough to the high-frequency cabling.

C. High-frequency antenna

The implementation of the dedicated high-frequency line requires a solution for coupling the high-frequency signal to the tunnel junction. We designed an antenna to transform the electric signal in the high-frequency line into electro-magnetic radiation illuminating the tunnel junction, with the STM tip effectively acting as a receiver. A dedicated antenna ensures efficient coupling into the vacuum reducing losses. Mounting it in close proximity to the tunnel contact further improves the signal strength.

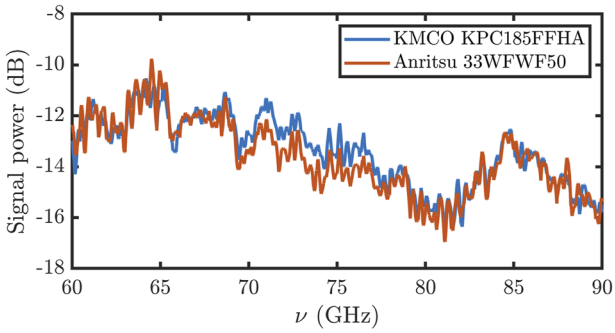

FIG. 2. Transmission through the 1.85 mm feedthrough KPC185FFHA, rated to 65 GHz, (blue) and the 1 mm female–female adapter 33WFWF50, rated to 110 GHz. Both components have comparable losses in the frequency range of interest.

We chose an on-chip antenna design for a compact and integrated solution.[22] For details on antenna theory, please see Refs. 23–25. The silicon chip is mounted in a phosphorous bronze carrier attached directly to the side of the STM scanner housing, shown in Fig. 3(a). A flange mount connector (Anritsu W1-103F) provides the electrical contact to the high-frequency wiring. To increase the microwave power incident on the tunnel junction, we fitted the carrier with a hyper-hemispherical silicon lens flush with the underside of the antenna chip to partially collimate the radiation. The antenna is mounted 14 mm away from the tunnel junction (the shortest distance between the lens and the tip) such that there is enough free space for tip and sample transfer. Although the antenna is placed in close proximity to the tunnel junction due to size constraints, we approximate the tunnel junction to be in the radiating

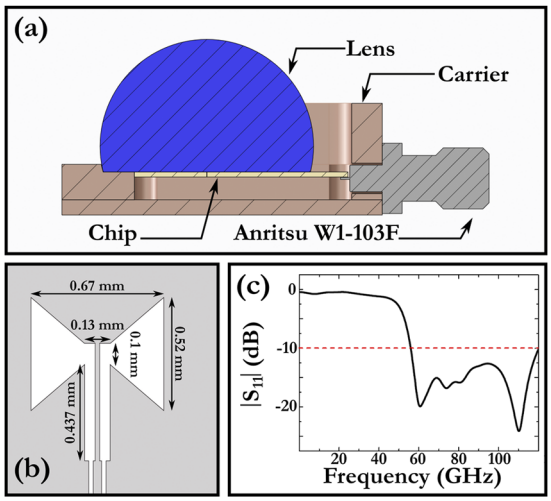

FIG. 3. Antenna design: (a) Sectional drawing of the antenna carrier with the lens installed. (b) Scale drawing of the antenna. Gray areas denote the AuPd layer. The antenna is assembled on a 10 × 20 mm^2 high resistivity silicon chip. (c) Simulated reflectance of the antenna up to 120 GHz. The antenna achieves excellent power dissipation across a wide band beginning at about 60 GHz.

near-field/Fresnel-region[25] of the antenna assembly following its characteristic dimensions and the small wavelength of the signal. As such, we assume a farfield-like behavior of the antenna to be the dominating means of RF-power delivery. Applying the Friis transmission equation,[25] this results in a purely $1/R^2$ decrease in signal power as the distance R between the antenna and tunnel junction increases.

A broadband bowtie antenna affords the most flexibility, covering the entire intended frequency range of 60–90 GHz. Figure 3(b) shows a dimensional drawing of the optimized antenna structure installed in the microscope. The orientation of the antenna is such that the vertical symmetry line is parallel to the tip. The antenna is assembled in a thin AuPd film on a high resistivity silicon substrate of 380 μm thickness. Design and parameter optimization for the antenna was performed using the CST Microwave Studio software with performance tests in 8.4:1 scale models. Figure 3(c) shows the simulated reflectance of the antenna from DC up to 120 GHz.[22] The design achieves excellent power dissipation across a wide band beginning at about 60 GHz.

III. RADIO FREQUENCY GENERATION

We use a multi-stage generation scheme to reach our intended operational frequency window [see Fig. 1(b)]. The first stage is a base band generator (Keysight 8257D) capable of producing signals up to 20 GHz. This generator feeds a frequency extension module (VDI WR12SGX), which multiplies the input frequency by a factor of six. The frequency extension module is intended to operate with input frequencies between 10 GHz and 15 GHz, producing a constant amplitude signal between 60 GHz and 90 GHz. We found that the upper limit can be extended by feeding the module with higher input frequencies, but at a significant cost in amplitude. Still, overdriving allows us to extend the operational frequency range of our ESR-STM to 105 GHz. Expanding the frequency range at the lower end in the same fashion is not possible due to the sharp cut-off of the WR12 waveguide output on the extension module. The output of the frequency extension module cannot be regulated. It provides a constant power of 16 dBm (about 40 mW), which translates to an amplitude of about 2 V. We regulate the source amplitude through a computer-controlled rotary vane attenuator (Mi-Wave 511E/387ND). This device allows us to regulate the power entering the high-frequency wiring in steps of 0.1 dB from the source power of the frequency extension module.

IV. INSTRUMENT PERFORMANCE

Key operational parameters of the instrument, such as base temperature, z-stability, and ^{3}He hold time, were unaffected by our modifications. We demonstrate the excellent STM performance in a series of test measurements on V(100). Figure 4(a) shows the oxygen reconstruction of the V(100) surface[26,27] in atomic resolution at the base temperature of 310 mK after the system upgrade. Tunneling spectroscopy between a superconducting vanadium tip and the V(100) sample shows well-developed coherence peaks and a clear energy gap typical of superconductor–insulator–superconductor junctions [see Fig. 4(b)].[21,28,29]

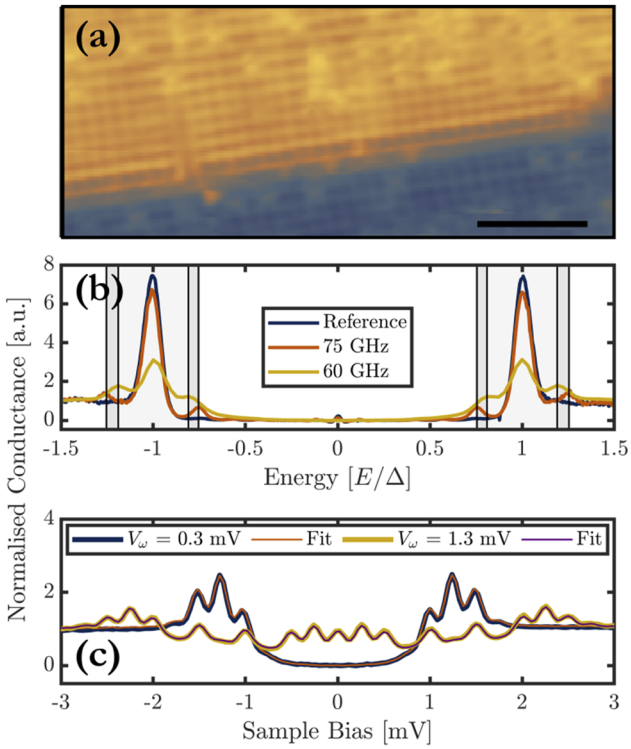

FIG. 4. Performance test using a superconductor–insulator–superconductor (SIS) tunnel junction. (a) Atomic resolution image of the oxygen reconstruction on a V(100) surface. The scale bar indicates 2 nm. (b) A typical reference spectrum of the SIS contact in the absence of an RF signal (blue) is shown alongside conductance spectra under irradiation by a RF signal of 75 GHz (orange) and 60 GHz (yellow). Replica of the superconducting coherence peaks is clearly resolved. Their separation from the original position depends on the frequency of the RF signal. The energy axis is referenced to the sum of the superconducting gaps $\Delta = \Delta_1 + \Delta_2$, where $\Delta_1 = 0.76$ mV and $\Delta_2 = 0.56$ mV. (c) Experimental data for a junction under irradiation by 60 GHz radiation of varying power (blue and yellow) with fits from the model in Eq. (1) superimposed (orange and purple).

A. Microwave signal delivery

We evaluate the performance of the microwave assembly by observing microwave-assisted tunneling processes occurring in a superconductor–insulator–superconductor (SIS) junction between a V(100) sample and a vanadium tip driven by a high-frequency signal from the antenna. SIS junctions are well studied and a robust framework for data analysis is readily available.[19,30–32] The current in the presence of a radio frequency signal is[30,33]

$$I_{\mathrm{QP}}(V_0, V_\omega) = \sum_{n=-\infty}^{\infty} J_n^2\left(\frac{eV_\omega}{\hbar\omega}\right) I_{\mathrm{QP}}\left(V_0 - \frac{n\hbar\omega}{e}, 0\right), \qquad (1)$$

where $I_{\mathrm{QP}}(V,0)$ is the quasiparticle current in the absence of any RF radiation, V_0 is the DC bias voltage applied to the tunnel junction, V_ω is the AC voltage dropping across the junction as a result of the RF signal, J_n are the Bessel functions of the first kind of order n, and e is the elementary charge. Furthermore, $\hbar$ is the reduced Planck constant and $\omega = 2\pi\nu$, where ν is the microwave frequency. The sharp coherence peaks in the SIS tunnel data allow us to observe

directly the effects of changing frequency. To analyze our data, we use reference spectra acquired using the same parameters as the corresponding microwave-assisted tunneling spectrum, but with the RF signal switched off. This reference measurement is used as the input for I_{QP} in Eq. (1). Fitting our model to the experimental data allows us to extract the frequency and amplitude of the RF signal arriving at the junction. All data shown are acquired at a base temperature of 310 mK.

Figure 4(b) shows a typical conductance spectrum of the SIS junction in blue. We observe two prominent coherence peaks separated by twice the sum of the superconducting gaps of the tip and sample. At zero bias voltage, a small supercurrent flows through the junction as a result of the Josephson effect, proving that both the tip and sample are in the superconducting state. The orange and yellow lines show conductance spectra of the SIS junction under the influence of RF radiation of 75 GHz and 60 GHz, respectively. Microwave driving of the junction gives rise to replica of the coherence peaks, offset by integer multiples of $h\nu$ from the main features and weighted by the square of the corresponding Bessel function.

We fit our data with the model given in Eq. (1) to extract the AC voltage dropping across the RF driven junction. Figure 4(c) shows sample fits for a junction under irradiation by 60 GHz radio waves. As the RF power and hence the AC voltage drop across the SIS junction increase, higher order processes become visible. As the total current through the junction remains the same, microwave-assisted tunneling leads to an overall decrease in the heights of individual peaks as the spectral weight is redistributed across a wide voltage range. The fitted curves are in excellent agreement with the data. Only a single frequency is needed in the model to reproduce the experimental results.[19]

B. ESR-STM

The prototypical spin systems for ESR-STM are individual metal atoms on an MgO decoupling layer on Ag(100).[3] We grow double-layer MgO islands by sublimation of Mg in a 1×10^{-6} mbar oxygen atmosphere onto the sample held at 700 K. Sublimation of Ti and Fe from an electron beam evaporator onto the cold sample ($T \lesssim 20$ K) yields individual Fe atoms and TiH molecules. We use individual metal atoms on MgO/Ag(100) as a model system to provide proof of principle ESR-STM measurements. Figure 5(a) shows an STM topograph of a typical sample, once again demonstrating that the machine can resolve single atoms with ease. The tip is a sharpened PtIr wire, further prepared by field emission in the microscope and repeated indentation into the Ag(100). We identify individual Fe atoms and TiH molecules through their fingerprints using inelastic excitation tunnel spectroscopy (IETS); see Figs. 5(b) and 5(c).

The essential ingredient of any ESR measurement is the tuning of the spin system across its resonance with the microwave signal. This may be achieved through either changing the excitation frequency at a fixed field (ν sweep), or the external field at a fixed excitation frequency (B sweep). In either case, it is necessary to calibrate the microwave amplitude in order to perform consistent and comparable measurements. Frequency sweeps further require the compensation of the antenna–junction transfer function to ensure a constant amplitude signal throughout the measurement to suppress spurious signals.

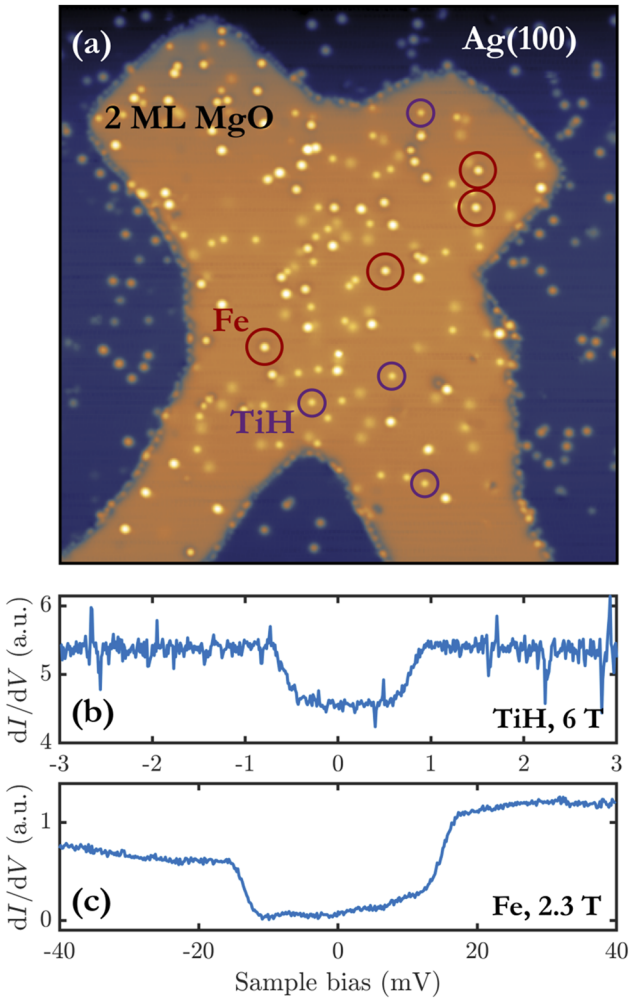

FIG. 5. Individual atoms on a thin insulating layer for ESR-STM experiments. (a) A double layer MgO island on an Ag(100) surface serves as a decoupling layer for individual Fe atoms and TiH molecules. (b) Inelastic excitation tunnel spectroscopy (IETS) spectrum on a TiH molecule in 6 T out of a plane external field. (c) IETS spectrum on an individual Fe atom in 2.3 T out of a plane external field. The width of the excitation gap around zero bias is a fingerprint for the unambiguous identification of Fe and TiH.

We mainly follow Ref. 15 to calibrate the microwave signal generate constant amplitude radio frequency sweeps at the junction. A similar procedure is given in Ref. 6. Individual TiH molecules on MgO show a prominent step-like feature at a bias voltage of about −80 mV [see the blue spectrum in Fig. 6(a)]. We first determine the transfer function of the antenna assembly at one fixed frequency using Eq. (1). We acquire a reference spectrum in the absence of any RF signal and a tunnel spectrum under RF irradiation, as for the SIS case above. Then, we extract the signal amplitude V_ω through a fit [see the yellow spectrum in Fig. 6(a)] of the data for the irradiated junction [see the red spectrum in Fig. 6(a)]. The transfer function T is then easily found from the known source amplitude V_S according to

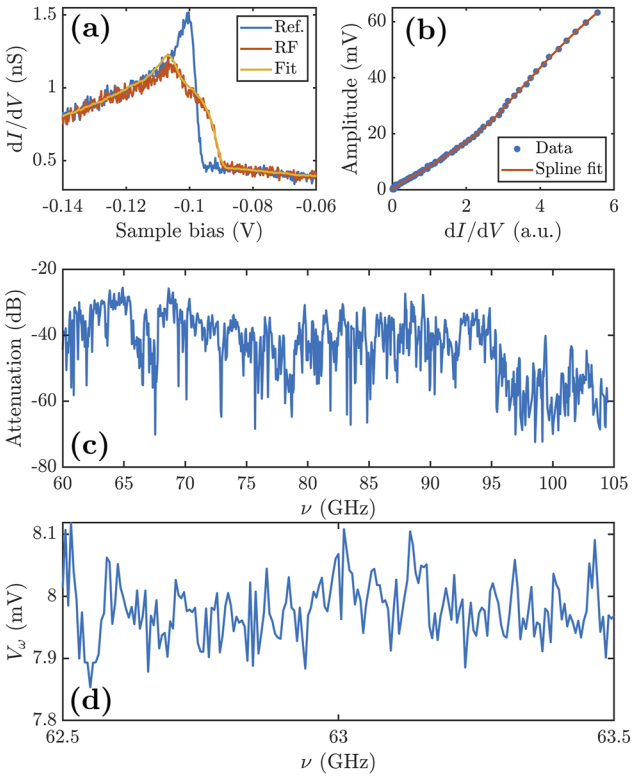

FIG. 6. Generation of constant amplitude radio frequency sweeps at the tunnel junction. (a) Step-like feature measured on a TiH molecule (blue), spectrum under radio frequency irradiation (orange), and fit using Eq. (1) (yellow) with $\nu = 64.9$ GHz and $V_\omega = 7.5$ mV. The radio frequency amplitude determined from the fit is used to compute the transfer function. (b) Calibration curve mapping the measured lock-in signal to RF amplitude. The orange line is a smoothed spline interpolation, which we use to interpolate the calibration curve. (c) Transfer function measured from 60 GHz to 105 GHz. The operational range of the instrument extends far past the intended 60–90 GHz. (d) Constant amplitude radio frequency sweep at 8 mV setpoint value.

$$T = 20\,\log(V_\omega/V_S). \tag{2}$$

We then acquire a calibration curve by measuring the conductance near the center of the slope of the TiH step as a function of source amplitude, see Fig. 6(b). We use a smoothing cubic spline interpolation to fit the calibration function more accurately for arbitrary shapes. The smoothing parameter must be calculated such that the resulting smoothed spline can be inverted. This produces better fits than directly fitting to the inverted data. With the known transfer function value, these values can be converted into signal amplitudes at the junction. Since the TiH step is much broader than $h\nu$ in the frequency range of interest, the frequency itself has no measurable effect on the RF spectrum and the calibration curve becomes a universal injective mapping of the conductance on V_ω.

By measuring the conductance of our tunnel junction with fixed signal attenuation while varying the source frequency and mapping the acquired values onto amplitudes using the inverted calibration curve, we measure the transfer function of the antenna assembly over a large frequency range, see Fig. 6(c). The instrument performs well over the complete intended operational range of 60–90 GHz and beyond. Losses do not become insurmountable until about 105 GHz. Using the experimentally determined transfer function, we can compensate the losses in the antenna assembly through the adjustable attenuator to generate constant amplitude radio frequency sweeps at the tunnel junction, see Fig. 6(d). We achieve signal amplitudes of 10 mV throughout most of the frequency range, and up to about 90 mV at select frequencies.

C. ESR signal

We demonstrate the ESR capabilities of our setup using TiH molecules on double layer MgO/Ag(100) as a model system (see Fig. 5). TiH adsorbed on the bridge site (between two oxygen atoms) of MgO is a spin-$\frac{1}{2}$ system with a g-factor close to 2 in an out-of-plane field.[6,34–37] We attach one or more Fe atoms to the STM tip to generate a spin-polarized probe by picking them up from the surface.[3] An out-of-plane magnetic field lifts the degeneracy between the spin states of the TiH molecule. In our frequency range, resonance is achieved in fields between about 2.15 T and 3.75 T. The Zeeman energy in these fields is about an order of magnitude larger than the thermal energy at the base temperature of 310 mK and the spin systems are thermally initialized to their ground state. All of the data presented here are measured at a bias voltage of 100 mV, and the setpoint currents are referenced to this voltage.

The RF signal drives the resonant transition between the ground and excited states, resulting in a reduction in the spin-polarized signal on the atom as the time-averaged spin population is no longer thermal. By chopping the RF driving signal and locking in to the chopping frequency with a lock-in amplifier, we single out and record those parts of the signal that are affected by the driving, i.e., the ESR-STM signal.[3,15]

Our results are summarized in Fig. 7. All data shown were acquired with the same spin-polarized microtip on the same TiH molecule adsorbed on a bridge site. Figures 7(a) and 7(b) show frequency sweep ESR-STM measurements at 175 pA and 50 pA setpoint currents, respectively. The RF amplitudes are 10 mV and 15 mV for the data at 175 pA and 50 pA, respectively. We find intervals throughout the frequency band between 60 GHz and 95 GHz, where the transmission is high enough such that a ν sweep is possible (as indicated in the insets). As the probe current is itself a source of decoherence, the linewidth is substantially reduced at lower current. This reproduces the general trend that has been observed previously.[4] In addition, the line widths of the measured ESR peaks are comparable to the published literature at lower frequencies (≤40 GHz).

Figure 7(c) shows ESR data from B sweep measurements at 16 different excitation frequencies spanning the available frequency range between 60 GHz and 100 GHz of the instrument. The microwave amplitude was set to 10 mV. The baseline has been offset to zero for all sweeps. We find a fairly even distribution of microwave frequencies with high enough amplitude for ESR spectroscopy across a magnetic field range spanning almost 1.5 T. Such a spread allows for a more accurate determination of the g-factor, which contains valuable information on the molecule and its environment.[36]

We calculate the corresponding Zeeman energies $E_Z = h\nu_{res}$ for all datasets, where ν_{res} is the resonance frequency. The g-factor of

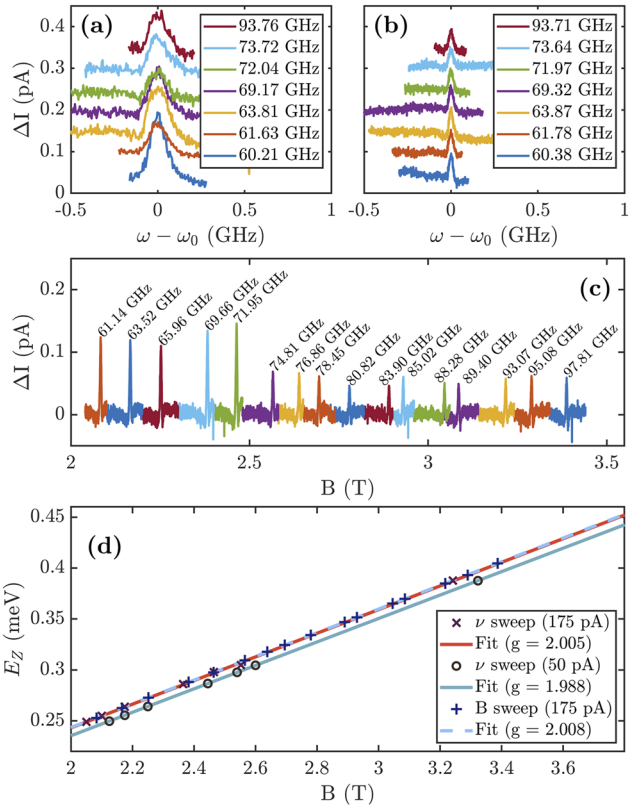

FIG. 7. High-frequency ESR-STM. ESR-STM signals from frequency sweeps at 175 pA (a) and 50 pA (b) setpoint current. The legend gives the center frequency of the signal. The probe current is a source of decoherence that contributes to the broadening of the signal. (c) ESR-STM signals from field sweeps at 175 pA setpoint current. The frequency of the excitation signal for each sweep is given in the annotations. (d) All ESR-STM measurements yield a *g*-factor close to 2.

our spin system can then be extracted through a simple linear fit according to

$$E_Z = 2\mu_B s g B, \tag{3}$$

where μ_B is the Bohr magneton and $s = 1/2$ is the spin of the TiH molecule. The results are shown in Fig. 7(d). We consistently obtain *g*-factors close to 2 for all our measurements, in agreement with previous results for TiH on the bridge site and in an out-of-plane field.[6] The data points lie very well on the line given by Eq. (3) for both the ν sweep as well as the B sweep, which were extracted from independent measurements at 175 pA setpoint current shown in Figs. 7(a) and 7(c). The fitted *g*-factors are $g = 2.005$ (ν sweep) and $g = 2.008$ (B sweep), which lie within 0.15%. For the ν sweep at 50 pA setpoint current, we find a *g*-factor of $g = 1.988$, which is slightly smaller than that for the higher setpoint current. The offset between the ν sweeps at 50 pA and 175 pA setpoint currents can be attributed to the different tip fields B_{tip} felt by the TiH molecule. The tip fields are 95.7 mT (B sweep) and 95.1 mT (ν sweep) at the 175 pA current setpoint and 46.1 mT for the 50 pA current setpoint. The small changes in the *g*-factor can be attributed to tip-induced changes in the TiH bond length.[36,37]

V. CONCLUSION

We have augmented a commercially available low-temperature STM system into a high-performance ESR-STM by the addition of a dedicated high-frequency line with antenna assembly to deliver radio frequency signals between 60 GHz and 105 GHz to the tunnel junction. Using commercially available components rated to high GHz frequencies, we achieve a high signal amplitude across a wide frequency range. The compensation of the transfer function allows us to keep the signal amplitude constant throughout our frequency range. In a series of proof-of-principle measurements, we measure an ESR signal on individual TiH molecules on a MgO decoupling layer in both frequency sweep and field sweep modes. In an operational field of several tesla and at a base temperature of 310 mK, excited state populations of typical spin-$\frac{1}{2}$ systems at a resonance frequency above 60 GHz are lower than 0.01%. With these parameters, it becomes possible to study the intrinsic dynamics of individual spins with atomic resolution. Going beyond the Zeeman splitting, the high frequencies translate to energies of up to 0.4 meV so that the observation of transitions between multiplets in atoms and nanostructures becomes possible. Our approach can serve as a template to convert typical STMs into ESR-STMs capable of resolving the coherent dynamics of individual spins and magnetic nanostructures.

ACKNOWLEDGMENTS

We thank Andreas Heinrich, Klaus Kern, Aparajita Singha, Markus Ternes, and Philip Willke for fruitful discussions. This work was funded in part by the ERC Consolidator Grant AbsoluteSpin (Grant No. 681164).

AUTHOR DECLARATIONS

Conflict of Interest

The authors have no conflicts to disclose.

DATA AVAILABILITY

The data that support the findings of this study are available from the corresponding author upon reasonable request.

REFERENCES

[1] A. J. Heinrich, J. A. Gupta, C. P. Lutz, and D. M. Eigler, "Single-atom spin-flip spectroscopy," Science **306**, 466 (2004).
[2] C. F. Hirjibehedin, C.-Y. Lin, A. F. Otte, M. Ternes, C. P. Lutz, B. A. Jones, and A. J. Heinrich, "Large magnetic anisotropy of a single atomic spin embedded in a surface molecular network," Science **317**, 1199 (2007).
[3] S. Baumann, W. Paul, T. Choi, C. P. Lutz, A. Ardavan, and A. J. Heinrich, "Electron paramagnetic resonance of individual atoms on a surface," Science **350**, 417 (2015).
[4] P. Willke, W. Paul, F. D. Natterer, K. Yang, Y. Bae, T. Choi, J. Fernández-Rossier, A. J. Heinrich, and C. P. Lutz, "Probing quantum coherence in single-atom electron spin resonance," Sci. Adv. **4**, eaaq1543 (2018).
[5] K. Yang, W. Paul, S.-H. Phark, P. Willke, Y. Bae, T. Choi, T. Esat, A. Ardavan, A. J. Heinrich, and C. P. Lutz, "Coherent spin manipulation of individual atoms on a surface," Science **366**, 509 (2019).
[6] T. S. Seifert, S. Kovarik, C. Nistor, L. Persichetti, S. Stepanow, and P. Gambardella, "Single-atom electron paramagnetic resonance in a scanning tunneling microscope driven by a radio-frequency antenna at 4 K," Phys. Rev. Res. **2**, 013032 (2020).

[7]L. M. Veldman, L. Farinacci, R. Rejali, R. Broekhoven, J. Gobeil, D. Coffey, M. Ternes, and A. F. Otte, "Free coherent evolution of a coupled atomic spin system initialized by electron scattering," Science **372**, 964 (2021).
[8]A. V. Balatsky, M. Nishijima, and Y. Manassen, "Electron spin resonance-scanning tunneling microscopy," Adv. Phys. **61**, 117 (2012).
[9]S. Müllegger, S. Tebi, A. K. Das, W. Schöfberger, F. Faschinger, and R. Koch, "Radio frequency scanning tunneling spectroscopy for single-molecule spin resonance," Phys. Rev. Lett. **113**, 133001 (2014).
[10]G. Binnig, H. Rohrer, C. Gerber, and E. Weibel, "Surface studies by scanning tunneling microscopy," Phys. Rev. Lett. **49**, 57 (1982).
[11]S. Loth, M. Etzkorn, C. P. Lutz, D. M. Eigler, and A. J. Heinrich, "Measurement of fast electron spin relaxation times with atomic resolution," Science **329**, 1628 (2010).
[12]T. L. Cocker, V. Jelic, M. Gupta, S. J. Molesky, J. A. J. Burgess, G. D. L. Reyes, L. V. Titova, Y. Y. Tsui, M. R. Freeman, and F. A. Hegmann, "An ultrafast terahertz scanning tunnelling microscope," Nat. Photonics **7**, 620 (2013).
[13]S. Yoshida, Y. Aizawa, Z.-h. Wang, R. Oshima, Y. Mera, E. Matsuyama, H. Oigawa, O. Takeuchi, and H. Shigekawa, "Probing ultrafast spin dynamics with optical pump–probe scanning tunnelling microscopy," Nat. Nanotechnol. **9**, 588 (2014).
[14]R. Gutzler, M. Garg, C. R. Ast, K. Kuhnke, and K. Kern, "Light–matter interaction at atomic scales," Nat. Rev. Phys. **3**, 441–453 (2021).
[15]W. Paul, S. Baumann, C. P. Lutz, and A. J. Heinrich, "Generation of constant-amplitude radio-frequency sweeps at a tunnel junction for spin resonance STM," Rev. Sci. Instrum. **87**, 074703 (2016).
[16]F. D. Natterer, F. Patthey, T. Bilgeri, P. R. Forrester, N. Weiss, and H. Brune, "Upgrade of a low-temperature scanning tunneling microscope for electron-spin resonance," Rev. Sci. Instrum. **90**, 013706 (2019).
[17]J. Friedlein, J. Harm, P. Lindner, L. Bargsten, M. Bazarnik, S. Krause, and R. Wiesendanger, "A radio-frequency spin-polarized scanning tunneling microscope," Rev. Sci. Instrum. **90**, 123705 (2019).
[18]W. M. J. van Weerdenburg, M. Steinbrecher, N. P. E. van Mullekom, J. W. Gerritsen, H. von Allwörden, F. D. Natterer, and A. A. Khajetoorians, "A scanning tunneling microscope capable of electron spin resonance and pump–probe spectroscopy at mK temperature and in vector magnetic field," Rev. Sci. Instrum. **92**, 033906 (2021).
[19]P. Kot, R. Drost, M. Uhl, J. Ankerhold, J. C. Cuevas, and C. R. Ast, "Microwave-assisted tunneling and interference effects in superconducting junctions under fast driving signals," Phys. Rev. B **101**, 134507 (2020).
[20]M. Assig, M. Etzkorn, A. Enders, W. Stiepany, C. R. Ast, and K. Kern, "A 10 mK scanning tunneling microscope operating in ultra high vacuum and high magnetic fields," Rev. Sci. Instrum. **84**, 033903 (2013).
[21]M. Tinkham, *Introduction to Superconductivity* (Dover, 1996).
[22]J. Merkt, "Entwurf und untersuchung einer antenne für 84 GHz zur strahlungseinkopplung in ein STM," B.Sc. thesis, Karlsruher Institut für Technologie, 2017.
[23]M. J. M. van der Vorst, "Integrated lens antennas for submillimetre-wave applications," Ph.D. thesis, Eindhoven University of Technology, 1999.
[24]A. Scheuring, "Ultrabreitbandige strahlungseinkopplung in THz-detektoren," Ph.D. thesis, Karlsruher Institut für Technologie, 2013.
[25]C. A. Balanis, *Antenna Theory*, 4th ed. (John Wiley & Sons, 2016).
[26]P. W. Davies and R. M. Lambert, "Surface chemistry of the metal-halogen interface: Bromine chemisorption and related studies on vanadium (100)," Surf. Sci. **95**, 571 (1980).
[27]J. S. Foord, A. P. C. Reed, and R. M. Lambert, "The (100) surfaces of chromium and vanadium: Reconsiderations of their structure and reactivity," Surf. Sci. **129**, 79 (1983).
[28]C. R. Ast, B. Jäck, J. Senkpiel, M. Eltschka, M. Etzkorn, J. Ankerhold, and K. Kern, "Sensing the quantum limit in scanning tunnelling spectroscopy," Nat. Commun. **7**, 13009 (2016).
[29]B. Jäck, M. Eltschka, M. Assig, M. Etzkorn, C. R. Ast, and K. Kern, "Critical Josephson current in the dynamical Coulomb blockade regime," Phys. Rev. B **93**, 020504 (2016).
[30]G. Falci, V. Bubanja, and G. Schön, "Quasiparticle and Cooper pair tunneling in small capacitance Josephson junctions," Z. Phys. B: Condens. Matter **85**, 451 (1991).
[31]A. Roychowdhury, M. Dreyer, J. Anderson, C. Lobb, and F. Wellstood, "Microwave photon-assisted incoherent Cooper-pair tunneling in a Josephson STM," Phys. Rev. Appl. **4**, 034011 (2015).
[32]O. Peters, N. Bogdanoff, S. Acero González, L. Melischek, J. R. Simon, G. Reecht, C. B. Winkelmann, F. von Oppen, and K. J. Franke, "Resonant Andreev reflections probed by photon-assisted tunnelling at the atomic scale," Nat. Phys. **16**, 1222 (2020).
[33]P. K. Tien and J. P. Gordon, "Multiphoton process observed in the interaction of microwave fields with the tunneling between superconductor films," Phys. Rev. **129**, 647 (1963).
[34]Y. Bae, K. Yang, P. Willke, T. Choi, A. J. Heinrich, and C. P. Lutz, "Enhanced quantum coherence in exchange coupled spins via singlet-triplet transitions," Sci. Adv. **4**, eaau4159 (2018).
[35]K. Yang, Y. Bae, W. Paul, F. D. Natterer, P. Willke, J. L. Lado, A. Ferrón, T. Choi, J. Fernández-Rossier, A. J. Heinrich, and C. P. Lutz, "Engineering the eigenstates of coupled spin-1/2 atoms on a surface," Phys. Rev. Lett. **119**, 227206 (2017).
[36]M. Steinbrecher, W. M. J. van Weerdenburg, E. F. Walraven, N. P. E. van Mullekom, J. W. Gerritsen, F. D. Natterer, D. I. Badrtdinov, A. N. Rudenko, V. V. Mazurenko, M. I. Katsnelson *et al.*, "Quantifying the interplay between fine structure and geometry of an individual molecule on a surface," Phys. Rev. B **103**, 155405 (2021).
[37]T. S. Seifert, S. Kovarik, D. M. Juraschek, N. A. Spaldin, P. Gambardella, and S. Stepanow, "Longitudinal and transverse electron paramagnetic resonance in a scanning tunneling microscope," Sci. Adv. **6**, eabc5511 (2020).